

## MATERIALS SCIENCE

# Establishing gas transport highways in MOF-based mixed matrix membranes

Conger Li<sup>1</sup>, Anheng Qi<sup>1</sup>, Yang Ling<sup>1</sup>, Yu Tao<sup>1</sup>, Yue-Biao Zhang<sup>1,2</sup>, Tao Li<sup>1\*</sup>

Achieving percolation pathways in a metal-organic framework (MOF)-based mixed matrix membrane (MMM) without compromising its mechanical properties is challenging. We developed phase separated (PS)-MMMs with an interconnected MOF domain running across the whole membrane. Through demixing two immiscible polyimides, the MOF particles were selectively partitioned into one of the preferred polymer domains at over 50 volume % local packing density, leading to a percolated network at only 19 weight % MOF loading. The CO<sub>2</sub> permeability of this PS-MMM is 6.6 times that of the pure polymer membrane, while the CO<sub>2</sub>/N<sub>2</sub> and CO<sub>2</sub>/CH<sub>4</sub> selectivity remain largely unchanged. Meanwhile, benefiting from its unique co-continuous morphology, the PS-MMM also exhibited markedly improved membrane ductility compared to the conventional MMM at similar MOF loading. PS-MMMs offer a practical solution to simultaneously achieve high membrane permeability and good mechanical properties.

## INTRODUCTION

Large-scale industrial separations of chemical feedstocks are generally realized through energy-intensive processes such as cryogenic distillation and adsorptive separation. As an energy-efficient alternative, membrane separation has attracted broad interest in academia and in industry (1, 2). Nonetheless, compared to the total chemical separation demand, membrane separation only accounts for a small fraction of the market. For instance, the CO<sub>2</sub> removal market in 2017 was dominated by the inefficient amine processes, whereas membrane only contributed 8% (3, 4). The major limiting factor that prevents membrane technologies to be more widely applied is the subpar performance of the polymeric membranes that are insufficient to address many separation challenges. As revealed in the renowned Robeson's upper-bound relationship, polymeric membranes exhibit a clear trade-off between their permeability and selectivity (5–7). To subdue the performance barrier of polymeric membranes, highly permeable and selective porous fillers are commonly introduced and dispersed in polymer matrixes to endow the membranes with enhanced separation performance. These types of membranes are known as mixed matrix membranes (MMMs) (8–12).

Among vast selections of filler materials, metal-organic frameworks (MOFs) have been the central pursuit because of their tunable chemical, structural, and morphological features (13–18). To date, although MOF-based MMMs have found continuous success in enhancing the gas separation performance of their polymer counterparts, it is still nowhere near the theoretical capability of pure MOF membranes (19–25). Aside from the interfacial factors, the main bottleneck is the lack of a continuous transport pathway in the membrane, as the filler particles are always separated by the less permeable polymer (26–28).

One way to address this issue is to increase the loading of MOF particles to above a so-called percolation threshold [typically above 30 weight % (wt%)] to form a percolation network (29–31). For

instance, Su and co-workers (29) have found that when the UiO-66-NH<sub>2</sub> loading in the polysulfone membrane was increased from 30 to 40 wt%, a sudden boost of CO<sub>2</sub> permeability from 18 to 46 Barrer was observed, while the CO<sub>2</sub>/N<sub>2</sub> and CO<sub>2</sub>/CH<sub>4</sub> selectivities remained the same. This suggests the formation of a MOF percolation network in the MMM. Nevertheless, at a high MOF loading, the mechanical properties and the processability of the membranes are destined to suffer greatly to a point where the resultant membranes are no longer suitable for practical applications (32–35). Ideally, achieving a percolation network in a MOF-based MMM at low MOF loading can, in principle, harness the full separation potential of the MOF while maintaining the processability and mechanical advantages of the polymer matrix. This challenge has yet to be realized.

For long, uncontrolled MOF particle aggregation in MMMs is considered disadvantageous and needs to be avoided at all costs. This is because under most scenarios, particle aggregation is a direct consequence of poor interfacial compatibility, which is further associated with a high degree of defects at the interface (36–38). In this work, we prove that controlled rather than stochastic aggregation can not only avoid defect formation but also create percolation pathways in MMMs at only 19 wt% MOF loading. It is well-known that polymer blends can undergo phase separation to form co-continuous morphologies. By blending two immiscible polyimides (PIs) along with a zirconium MOF, UiO-66-NH<sub>2</sub>, in a good solvent, phase separation will occur upon solvent evaporation. The MOF particles will spontaneously segregate into the "preferred" polyimide phase. By systematically tuning the volume fraction of various components and the degree of phase separation, the MOF domains can be interconnected throughout the membrane. We name this type of membrane as phase separated (PS)-MMMs (Fig. 1A). At such low filler loading, the CO<sub>2</sub> permeability of the MMM was considerably increased while CO<sub>2</sub>/N<sub>2</sub> and CO<sub>2</sub>/CH<sub>4</sub> selectivities were largely maintained. Meanwhile, because of the presence of the continuous polymer phase, the MMM exhibited markedly improved ductility compared to the conventional MMM at the same MOF loading. The result highlights the

Copyright © 2023 The Authors, some rights reserved; exclusive licensee American Association for the Advancement of Science. No claim to original U.S. Government Works. Distributed under a Creative Commons Attribution NonCommercial License 4.0 (CC BY-NC).

<sup>1</sup>School of Physical Science and Technology, ShanghaiTech University, Shanghai 201210, China. <sup>2</sup>Shanghai Key Laboratory of High-Resolution Electron Microscopy, ShanghaiTech University, Shanghai 201210, China.

\*Corresponding author. Email: litao1@shanghaitech.edu.cn.

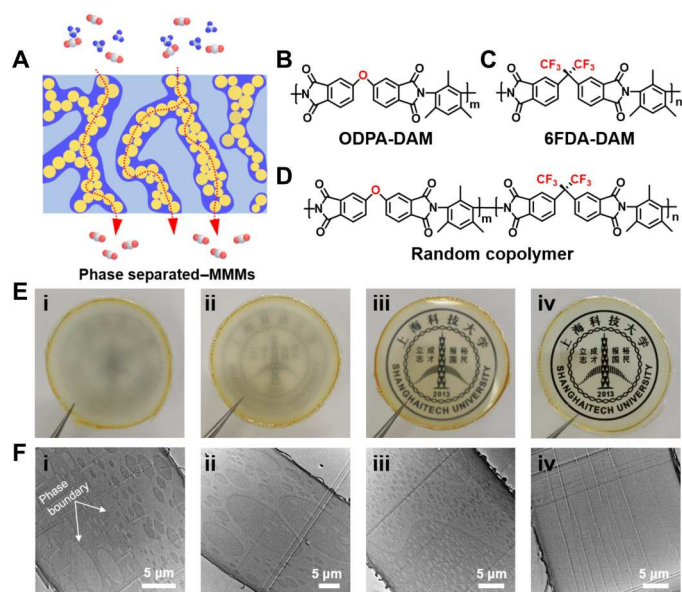


**Fig. 1. Controlling the phase separation of a PI blend.** (A) Schematic illustration of MOF percolation in PS-MMMs. (B to D) Structure of ODPA-DAM, 6FDA-DAM, and their RCP. Photographs (E) and TEM images (F) of the ultramicrotomed (100-nm-thick) samples of membranes obtained from solution casting of 1:1 mixture of ODPA-DAM and 6FDA-DAM (i), P1 and 6FDA-DAM (ii), P2 and 6FDA-DAM (iii), and P3 and 6FDA-DAM (iv).

possibility of achieving percolation and maintaining membrane flexibility at the same time.

## RESULTS

To start with, we first selected a pair of PIs, 4,4'-(hexafluoroisopropylidene) diphthalic anhydride (6FDA)-2,4,6-trimethyl-1,3-phenylenediamine (DAM) and 4,4'-oxidiphthalic anhydride (ODPA)-DAM, as the matrixes. Both PIs represent the state-of-the-art of PI materials for gas separation purposes (24, 39). In addition, by varying the ODPA-to-6FDA ratio in a random copolymer (RCP), its physical properties can be continuously tuned. This is a critical aspect to achieve the desired degree of phase separation for domain size control. Following a reported method, the neat 6FDA-DAM; ODPA-DAM; and three RCPs—(ODPA<sub>0.67</sub>/6FDA<sub>0.33</sub>)-DAM (P1), (ODPA<sub>0.50</sub>/6FDA<sub>0.50</sub>)-DAM (P2), and (ODPA<sub>0.33</sub>/6FDA<sub>0.67</sub>)-DAM (P3)—were synthesized (the subscripts represent the mole fraction of two anhydrides; figs. S1 to S4). Gel permeation chromatography (GPC) analysis revealed that the number-average molecular weight ( $M_n$ ) and dispersity ( $\mathcal{D}$ ) of the as-synthesized PIs are in the range of 38537 to 57881 and 1.64 to 2.01. Details are listed in table S1.

Next, we sought to investigate the miscibility of various polymer blends. Because of the polarity difference between ODPA and 6FDA segments (Fig. 1, B and C), the film obtained from solution casting of a 1:1 mixture of ODPA-DAM and 6FDA-DAM exhibited strong opacity (Fig. 1E, i). This indicates the occurrence of severe phase separation during the solvent evaporation process. By slicing the film using an ultramicrotome into 100-nm sections, the polymer

domains were clearly visible by transmission electron microscopy (TEM). Figure 1F (i) shows the phase separation occurred in two stages. First, two PIs separated into the top and bottom layers. Then, the minor PI component in each layer further nucleated into ellipsoid-shaped domains with an average size of  $\sim 5 \mu\text{m}$ . The contrast between two phases under TEM is likely a result of the presence of fluorine in 6FDA. (fig. S6). By replacing ODPA-DAM with P1, P2, and P3, the transparency of the film gradually increased (Fig. 1E, ii to iv), suggesting a lowering of phase separation tendency due to the increasing chemical similarity between two phases. This observation is further confirmed by the TEM images as the 6FDA-DAM/P1 and 6FDA-DAM/P2 blends no longer show top and bottom layer separation (Fig. 1F, ii and iii). In addition, the ellipsoid-shaped domains are also getting smaller. For the 6FDA-DAM/P3 blend, phase separation was not apparent under TEM (Fig. 1F, iv).

With four sets of PI blends ready, we shifted our attention to filler selection. A nanosized zirconium MOF, UiO-66-NH<sub>2</sub>, was selected for this investigation because of its ease of synthesis, size control, and proven ability for various gas separation applications (40, 41). Moreover, UiO-66-NH<sub>2</sub> is a prototypical MOF with isotropic micropore geometry and particle shape, which can simplify subsequent structural-property relationship analysis. In this context, monodispersed UiO-66-NH<sub>2</sub> particles with an average size of  $88 \pm 12 \text{ nm}$  were synthesized according to a previously reported method (fig. S7) (42).

To direct MOF particles into the desired polymer phase, UiO-66-NH<sub>2</sub> was first mixed and incubated with ODPA-DAM in dichloromethane (DCM) for 12 hours, allowing surface polymer physisorption to occur. After the addition of 6FDA-DAM, the solution was immediately casted onto a glass plate, and the solvent was allowed to slowly evaporate. The MOF, ODPA-DAM, and 6FDA-DAM were kept at a mass ratio of 1:4.5:4.5. As expected, the TEM image (Fig. 2A) revealed that UiO-66-NH<sub>2</sub> particles preferentially dispersed in a continuous polymer domain, whereas no MOF particles were found in the ellipsoid-shaped domain. Through energy dispersion x-ray spectroscopy (EDS) elemental mapping, it was found that the ellipsoid-shaped domain contains fluorine, whereas the continuous phase does not (Fig. 2A). This means all MOF particles were successfully incorporated in the ODPA-DAM phase as anticipated. If UiO-66-NH<sub>2</sub> was preincubated with 6FDA-DAM, then the MOF particles, instead of residing in the 6FDA-DAM phase, assembled into a densely packed monolayer at the phase boundary (Fig. 2B). This result indicates that the surface-adsorbed 6FDA-DAM may be partially exchanged by ODPA-DAM. Therefore, the MOF particles exhibited a surfactant-like behavior. It is also apparent that UiO-66-NH<sub>2</sub> has a higher affinity toward ODPA-DAM. Although it is difficult to distinguish two PI phases based on the TEM image, the EDS elemental mapping clearly outlined the spatial distribution of two polymers. To simplify the fabrication process of the PS-MMMs, UiO-66-NH<sub>2</sub> was directly mixed with both PIs. The resultant membrane showed well-separated PI phases with MOF particles solely residing in the ODPA-DAM domain (Fig. 2C). This protocol will be adopted for the later preparation of all PS membranes.

Nevertheless, because of the strong phase separation tendency between 6FDA-DAM and ODPA-DAM, the overall film still exhibits a double-layer morphology where one layer contains no MOF particles (Fig. 2D, i). This prevents MOF to form a percolation

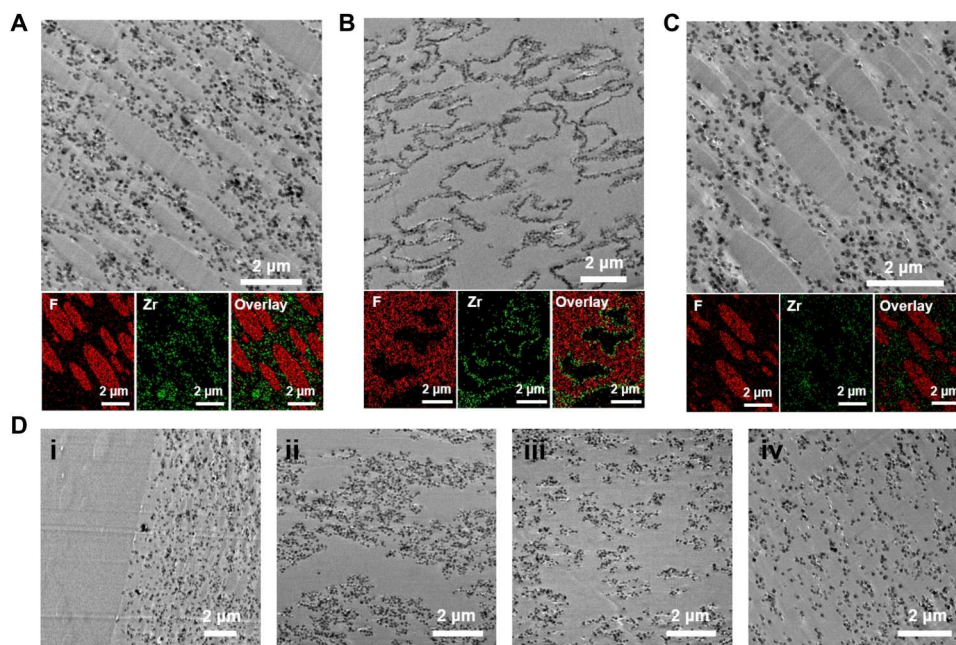


**Fig. 2. Allocating UiO-66-NH<sub>2</sub> particles in a PI blend.** TEM images and their corresponding EDS elemental mapping of the ultramicrotomed (100-nm-thick) samples of PS-MMMs prepared in different mixing sequences. (A) UiO-66-NH<sub>2</sub> was preincubated with ODPA-DAM for 12 hours before mixing with 6FDA-DAM. (B) UiO-66-NH<sub>2</sub> was preincubated with 6FDA-DAM for 12 hours before mixing with ODPA-DAM. (C) UiO-66-NH<sub>2</sub> was mixed with both PIs in one pot. TEM images of ultramicrotomed (100-nm-thick) samples of UiO-66-NH<sub>2</sub> dispersed in PI blends of ODPA-DAM/6FDA-DAM [(D), i], 6FDA-DAM/P1 [(D), ii], 6FDA-DAM/P2 [(D), iii], and 6FDA-DAM/P3 [(D), iv].

pathway throughout the membrane. To address this issue, ODPA-DAM was replaced by P1, P2, and P3 to slow down the phase separation process. The mass ratio between the MOF and two PIs was kept at 2:4:4. Because of the decrease of phase separation tendency, top and bottom layer separation was no longer observed (Fig. 2D, ii to iv). In addition, by increasing the mole fraction of the 6FDA segment in the RCP, the size of the MOF aggregates gradually decreased. Comparably, within the 6FDA-DAM/P1 blend, the MOF aggregates show moderate connectivity among each other (Fig. 2D, ii). Therefore, the 6FDA-DAM/P1 blend was selected as the matrix for further optimization.

To optimize the distribution of MOF domains, the mass ratio between P1, 6FDA-DAM, and MOF was further adjusted. Theoretically, to achieve a co-continuous polymer blend morphology requires a 1:1 (v/v) ratio between two immiscible phases. Therefore, the volume of the MOF phase (UiO-66-NH<sub>2</sub> + P1) should be equal or close to that of 6FDA-DAM. Hence, a new membrane was prepared with UiO-66-NH<sub>2</sub>, P1, and 6FDA-DAM mixed at a 2:3:5 (v/v) ratio. We denote this MMM as PS-19 [PS means “phase separated,” whereas 19 represents the actual MOF mass loading quantified by thermogravimetric analysis (TGA)]. Figure 3A shows that both the polymer phase and the MOF phase exhibited good long-range connectivity. The overall morphology resembles a co-continuous polymer blend structure. The domain size was in the range of 1 to 3 μm. Potential percolation pathways can be identified from one end of the membrane to the other end, with only occasional disconnections, as exemplified by the areas highlighted in yellow (Fig. 3A and fig. S8). Note that with the inclusion of out-of-plane connectivity under 3D format, the connectivity between individual MOF domains is expected to be higher than what is observed in the cross-sectional image. If the MOF loading was lowered to 13 wt%

(PS-13), then the MOF domains became less continuous, whereas the polymer phase remained continuous (Fig. 3B). On the other hand, if the MOF loading was increased to 23 wt% (PS-23) and 28 wt% (PS-28), the MOF domain remained continuous, whereas the polymer domains became less continuous (Fig. 3C and fig. S9).

The effect of MOF particle size on the morphologies of the PS-MMMs was also investigated. Apart from the 88-nm UiO-66-NH<sub>2</sub> previously synthesized, two UiO-66-NH<sub>2</sub> samples with average sizes of 180 and 320 nm and one UiO-66 sample with an average size of 600 nm were prepared (fig. S10). Following the same membrane fabrication protocol, similar co-continuous morphology was observed in the two PS-MMMs containing 180- and 320-nm UiO-66-NH<sub>2</sub>. In the PS-MMM containing 600-nm UiO-66 particles, the aggregation of UiO-66 particles was still apparent. However, large isolated ellipsoid-shaped P1 domain was observed. This is an indication of low MOF particle mobility. Consequently, the UiO-66 particles were loosely packed with poor domain connectivity.

In principle, this approach should be applicable to various types of MOFs and polymer blends so long as the polymer phase separation process can be systematically tuned. To demonstrate the generalizability of this method, two new MOFs, MOF-801 (~60 nm) and MIL-101(Cr)-NH<sub>2</sub> (~20 nm), were synthesized and incorporated into 6FDA-DAM/P1 blend at 5:3:2 volume ratio (6FDA-DAM:P1:MOF). TEM images show that both PS-MMMs exhibited co-continuous morphology resembling that of PS-19 (Fig. 4, A and B, and fig. S11). Similarly, both MOF-801 and MIL-101(Cr)-NH<sub>2</sub> preferably reside in the P1 phase. The results indicate that this approach can be potentially applied to a wide range of MOF fillers (fig. S12). To extend the polymer blend beyond 6FDA-DAM/P1, two other types of polymer blends were prepared for the construction

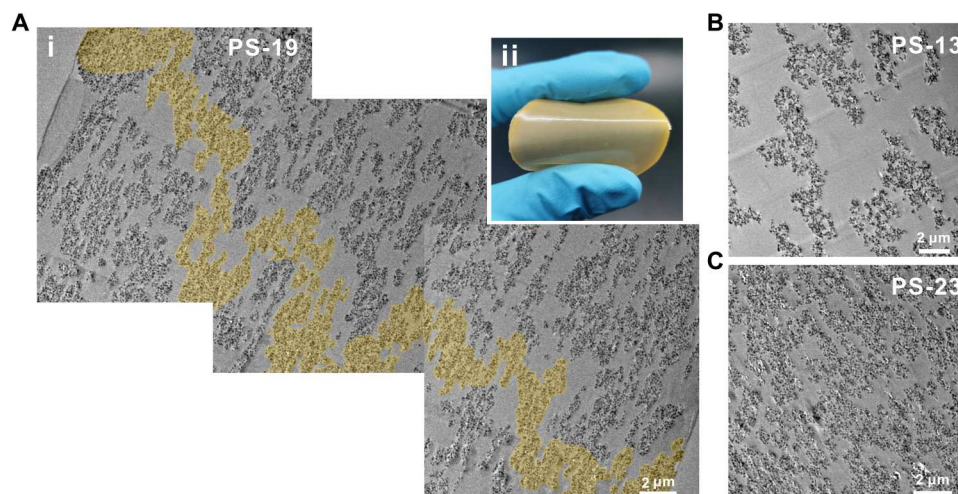


**Fig. 3. Percolation pathways in PS-MMMs.** TEM images of the ultramicrotomed (100-nm-thick) samples of [(A), i] PS-19, (B) PS-13, and (C) PS-23. The yellow line represents one potential percolation pathway in PS-19. [(A), ii] is a photograph of a bent PS-19 membrane.

of PS-MMMs. The first blend comprises 6FDA-DAM and an RCP 6FDA-(DAM<sub>0.85</sub>:DABA<sub>0.15</sub>) (DABA refers to 3,5-diaminobenzoic acid). The inclusion of DABA moiety into the PI creates chemical distinction that will facilitate phase separation. It was found that a DAM:DABA molar ratio of 5.7:1 can offer desired degree of phase separation. A mixture of 6FDA-DAM, 6FDA-(DAM<sub>0.85</sub>:DABA<sub>0.15</sub>), and UiO-66-NH<sub>2</sub> at 2:2:1 ratio also formed a PS-MMM exhibiting good MOF domain connectivity throughout the membrane (Fig. 4C). Apart from the RCP approach, commercial PIs can also

be incorporated in the matrix to yield PS-MMMs. An example is that the blend of ODPA-DAM, Matrimid@5218, and UiO-66-NH<sub>2</sub> at 2:2:1 ratio afforded a PS-MMM with excellent MOF particle connectivity (Fig. 4D). These examples fully demonstrated the generalizability of this approach.

On the basis of the examples demonstrated so far, there are four key parameters to achieve a MOF percolation network in PS-MMMs. First, the MOF surface must be preferably wetted by one polymer phase. This can be achieved with and without MOF surface modification. Second, the volume fraction of the MOF plus its preferred polymer phase should be equal or close to the secondary polymer phase. Third, small yet monodispersed MOF particles are desired to ensure sufficient mobility during phase separation. Last, the rate of phase separation should be systematically tuned by the polymer composition, MOF loading, and solvent evaporation rate.

For nonbiased comparison between PS membranes and non-PS (nPS) membranes, another RCP (ODPA<sub>0.25</sub>/6FDA<sub>0.75</sub>)-DAM (P4) was synthesized to match the chemical composition of 6FDA-DAM/P1 blend at 5:3 (v/v) ratio. In addition, nPS-MMMs with 10, 20, 29, and 35 wt% MOF loading were prepared using P4 as the matrix. These loading values were all quantified by TGA (fig. S13). For ease of discussion, these samples were denoted as nPS-10, nPS-20, nPS-29, and nPS-35, respectively. To quantitatively compare the interparticle distance in PS and nPS membranes, we analyzed and plotted the distributions of free path spacing (DFPS) for four samples (fig. S14). DFPS was a useful tool initially used by Luo and Koo to compare the particle dispersibility in various composites (43–45). In our case, the prerequisite to forming a percolated membrane is to have a low DFPS value, meaning gas molecules only have to pass through a thin barrier of polymer between particles. By increasing the MOF loadings from 10 to 35 wt% in nPS membranes, the peaks of the DFPS distribution decreased from ~200 to ~50 nm. However, even a 50-nm gap still presents a notable barrier for gas transport, given the fact that the MOF particle size is only ~88 nm. In shape contrast, the DFPS distribution of PS-13 and PS-19 are both peaked at ~20 nm, indicating a high degree of particle aggregation in the MMM (Fig. 5C). The

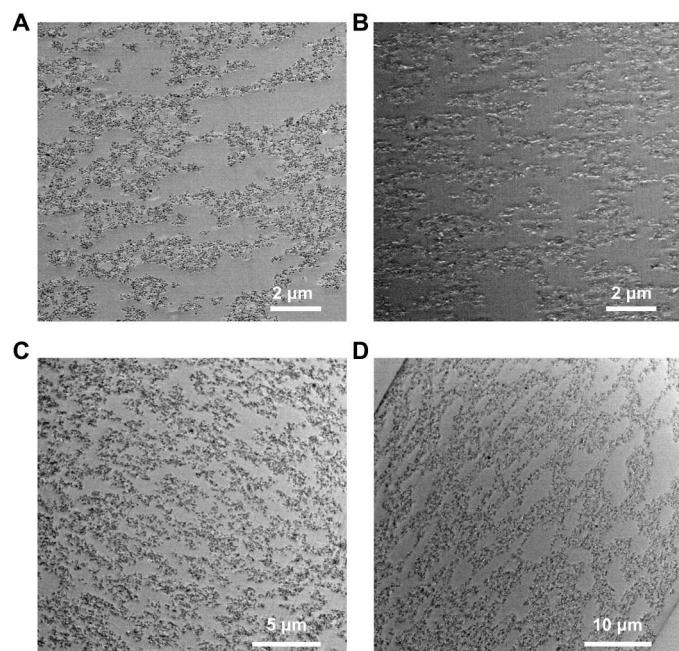


**Fig. 4. Expand the type of PS-MMMs.** TEM images of membrane ultrathin slices (100 nm) of (A) MOF-801 PS-MMM, (B) MIL-101(Cr)-NH<sub>2</sub> PS-MMM with the 6FDA-DAM/P1 blend, (C) 6FDA-DAM/6FDA-(DAM<sub>0.85</sub>:DABA<sub>0.15</sub>)/UiO-66-NH<sub>2</sub> polymer blend membrane with a ratio of 2:2:1, and (D) ODPA-DAM/Matrimid@5218/UiO-66-NH<sub>2</sub> polymer blend membrane with a ratio of 2:2:1.

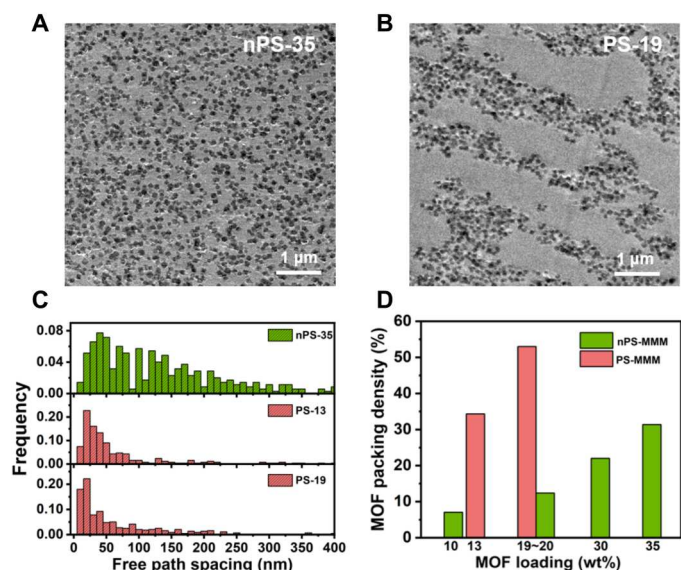


**Fig. 5. Statistical analysis of MOF packing density and spatial distribution.** TEM images of membrane ultrathin slices (100 nm) of (A) nPS-35 and (B) PS-19. (C) The DFPS for nPS-35, PS-13, and PS-19. (D) MOF packing density in nPS-MMMs (green columns) and MOF packing density (in the MOF domain) in PS-MMM (red). For clear visualization, the x axis is not plotted to scale.

packing density of the MOF in nPS and PS membranes (in the MOF domain) was quantitatively analyzed and calculated (Fig. 5D and fig. S15). With the increase of MOF loading in nPS membranes, the packing density steadily increased from 7% for nPS-10 to 31% for nPS-35. Notably, owing to the polymer phase separation, the MOF packing density in PS-13 and PS-19 reached 34 and 53%, respectively, far surpassing the packing density in the nPS membranes with comparable MOF loadings. The close proximity among particles along with the interconnectivity among neighboring MOF domains are two key features for achieving gas transport highways in the MMM.

To understand how the MMM morphology affects its mechanical properties, we performed tensile testing for the homopolymers, RCPs, nPS-MMMs, and PS-MMMs (Fig. 6A and fig. S16). The results show that the elongation at break (EAB) values for ODPA-DAM and 6FDA-DAM are 38.3 and 41.4%, respectively. The RCPs appeared to be less ductile, as their EAB values are at around 30%. This is likely due to their slightly lower molecular weight compared to the homopolymers (table S1). By incorporating 10 wt% UiO-66-NH<sub>2</sub> to P4, the EAB value quickly dropped to 7.9%. In comparison, PS-13 exhibited a slightly higher EAB value at 8.8% despite its higher MOF loading. Further increasing the MOF loading in an nPS-MMM to 20 wt% led to a drastic drop of EAB to only 1.9%. Just by lifting the nPS-20 membrane from the glass substrate had already caused cracking and fracturing (fig. S17A). Further increasing the MOF loading to 29 wt% led to a defective membrane too brittle to be freely handled. PS-19, on the other hand, exhibited a substantially higher EAB at 6.1%, markedly outperforming its nPS counterpart by 220%. One possible reason is that the continuous polymer phase in the PS-MMM serves as a buffer layer to arrest the propagation of cracking throughout the membrane. The Young's modulus and tensile strength of various membranes were calculated on the basis of the strain-stress curves and listed in table

S2. The results show that the Young's moduli of the PS-MMMs (PS-13 and PS-19) are slightly higher than that of the nPS-MMMs (nPS-10 and nPS-20). This is likely due to the presence of a rigid MOF domain in the PS-MMMs.

To gain more insight into the gas transport behavior in PS and nPS-MMMs, N<sub>2</sub>, CH<sub>4</sub>, and CO<sub>2</sub> pure gas transport experiments were performed at 35°C and 3 bar for pure polymer membranes and the MMMs (Fig. 6, B and D). The CO<sub>2</sub> permeability of two homopolymer membranes, 6FDA-DAM and ODPA-DAM, was 608 and 73 Barrer, respectively. As expected, P4 exhibited an intermediate CO<sub>2</sub> permeability at 210 Barrer. The CO<sub>2</sub>/N<sub>2</sub> selectivity of the three pure polymer membranes falls in the narrow range of 15 to 17. The 6FDA-DAM/P1 blend membrane, on the other hand, showed a slightly higher CO<sub>2</sub> permeability at 323 Barrer and lower CO<sub>2</sub>/N<sub>2</sub> selectivity at 13. This is likely due to the presence of continuous 6FDA-DAM channels in the 6FDA-DAM/P1 blend membrane and the defects.

Incorporating UiO-66-NH<sub>2</sub> into P4 at 10, 20, and 29 wt% led to a stepwise increase of CO<sub>2</sub> permeability from 210 to 316, 516, and 818 Barrer, respectively. On the contrary, the CO<sub>2</sub>/N<sub>2</sub> selectivity steadily decreased from 16 to 15, 14, and 11, respectively. These results agree well with our previous work (24). The lowering of the selectivity is likely a result of defect formation at the nonideal MOF-polymer interface. In contrast, with only 13 wt% MOF and local MOF domain connectivity, PS-13 exhibited a drastically increased CO<sub>2</sub> permeability of 538 Barrer, comparable to that of nPS-20. Benefiting from the co-continuous morphology, PS-19 manifested a remarkable CO<sub>2</sub> permeability of 1385 ± 111 Barrer. This value is ~6.6 times that of P4 and ~1.7 times that of nPS-29. The CO<sub>2</sub>/N<sub>2</sub> selectivity of PS-13 and PS-19 are 17 and 15, respectively, higher than their nPS counterparts and comparable to that of P4 (Fig. 6B). Further increasing the MOF loading to 28 wt% (PS-28) led to an even higher CO<sub>2</sub> permeability (1612 Barrer). However, the CO<sub>2</sub>/N<sub>2</sub> selectivity markedly decreased to 13. This is an indication of defect formation in the membrane, likely caused by overcrowding of MOF particles in the MOF domain.

For CO<sub>2</sub>/CH<sub>4</sub> separation, with the increase of MOF loading in the nPS-MMMs, the CO<sub>2</sub>/CH<sub>4</sub> selectivity decreased stepwise from 24 to 14, while the CO<sub>2</sub> permeability continuously increased. On the other hand, for the PS-MMMs, although the CO<sub>2</sub> permeability sharply increases, there is only a slight drop of CO<sub>2</sub>/CH<sub>4</sub> selectivity from 24 for P4 to 20 for PS-19. The CO<sub>2</sub>/CH<sub>4</sub> separation performance of PS-19 was positioned well above the 1991 Robeson upper bound and is approaching the 2008 upper bound (Fig. 6D). These results demonstrate a clear advantage of PS-MMM over conventional MMMs as the percolation pathway can lead to drastic enhancement of gas permeability even at a substantially lower loading. Because this aggregation process was not caused by incompatibility between the MOF and the polymer but rather the immiscibility of two polymers, favorable interaction is still attainable at the MOF-polymer interface.

Last, the high-pressure CO<sub>2</sub> and CH<sub>4</sub> adsorption isotherms were collected for P4, nPS-20, and PS-19 at 35°C (fig. S18). Combining with the permeability data of these membranes, the solubility (S) and diffusivity (D) values can be deconvoluted on the basis of the solution-diffusion model (Fig. 6C and table S3) (46). The incorporation of 20 wt% UiO-66-NH<sub>2</sub> into the polymer matrix increased the solubility of CH<sub>4</sub> and CO<sub>2</sub> by 46 and 33%, respectively. This is due to the preferential adsorption of two gases in UiO-66-NH<sub>2</sub>.

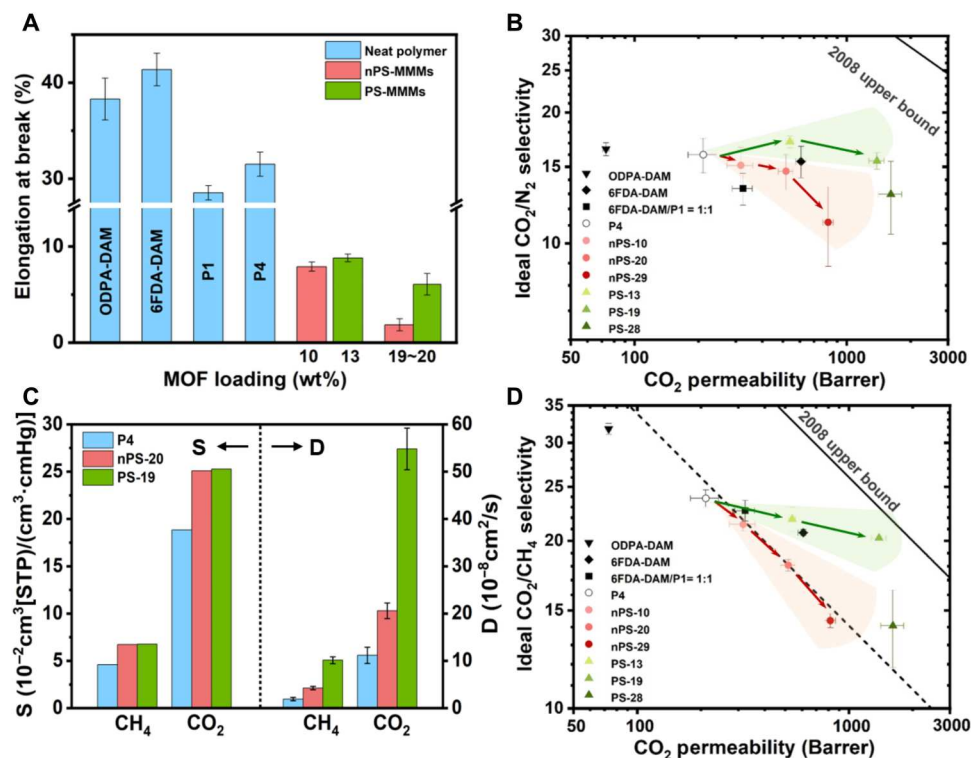


**Fig. 6. Mechanical and gas transport properties.** (A) The EAB values for the neat PI, RCPs, and MMMs. CO<sub>2</sub> permeability versus (B) CO<sub>2</sub>/N<sub>2</sub> selectivity and (D) CO<sub>2</sub>/CH<sub>4</sub> selectivity of pure polyimides, polyimide blend, RCP, nPS-MMMs, and PS-MMMs. (C) The solubility and diffusivity of CO<sub>2</sub> and CH<sub>4</sub> in P4, nPS-20, and PS-19 at 3 bar and 35°C.

Note that there is no appreciable solubility difference between nPS-20 and PS-19, meaning that morphological change does not affect gas solubility in membranes. In stark contrast, CO<sub>2</sub> and CH<sub>4</sub> diffusivity values in PS-19 are ~5 and ~2.5 times higher than P4 and nPS-20, respectively. This sudden boost in permeability can be attributed to the percolated MOF networks throughout the membrane.

Realistic gas separation applications demand high flux. Therefore, the composite membranes are typically made in the thickness range of hundreds of nanometers. It is thus highly valuable to investigate the possibility of fabricating sub-1- $\mu$ m PS-MMMs with percolation pathways. Because the solvent evaporation rate is much faster in thin-film composite (TFC) membranes than dense membranes, we mixed 6FDA-DAM, ODA-DAM, and UiO-66-NH<sub>2</sub> at a 2:2:1 ratio in a solvent mixture of *N,N'*-dimethylformamide (DMF) and DCM. The addition of DMF can slow down the solvent evaporation rate at the final stage, thus allowing longer phase separation period. The resultant TFC membrane exhibits islands of MOF nanoparticles in the size range of tens of micrometers under a scanning electron microscope (SEM; fig. S19). The cross-sectional image shows that the thickness of the membrane is ~1  $\mu$ m, whereas the MOF islands are slightly higher (2 to 3  $\mu$ m). Note that these MOF islands connect both ends of the membrane, hinting the presence of percolation pathways within the membrane. The preliminary result presented here demonstrates the potential of PS-MMMs under industrial settings. Although challenges still exist in forming defect-free co-continuous TFC membranes for gas separation, it is foreseeable that these issues can be addressed through future efforts such as optimizing the composition of the composites, interfacial modification, and perfecting the membrane fabrication process.

## DISCUSSION

Conventional wisdom tells us that the aggregation of MOF particles in MMMs is considered an unwelcomed event. This is because such aggregation is typically driven by the incompatibility at the MOF-polymer interface, which will further lead to interfacial defect and compromised gas separation performance. However, in this work, we demonstrated that controlled aggregation of MOF particles driven by the demixing of a polyimide blend can not only preserve a compatible MOF-polymer interface but also give rise to a unique co-continuous morphology with both the polymer and the MOF domain showing good continuity throughout the whole membrane. Through fine-tuning of various parameters such as MOF loading, polymer ratio, polymer composition, solvent evaporation rate, etc., local MOF packing density can reach as high as 53% (v/v), while the mean interparticle spacing is centered around 20 nm. Along with the high continuity between MOF domains, these unique morphological features effectively reduce the polymer barrier thickness among MOF particles, thus drastically increasing the CO<sub>2</sub> permeability of the MMM to 6.6 times that of the pure polymer membrane at only 19 wt% MOF loading. Moreover, benefiting from the continuous pure polymer phase presented in the membrane, the PS-MMM exhibited much higher ductility compared to conventional MMM at the same MOF loading. This feature is imperative for the deployment of MMMs in realistic application scenarios. Granted that PS-MMMs contain at least three components, the membrane morphology is influenced by numerous intertwined factors. Therefore, future efforts should be focused on fine tuning the membrane morphologies and understanding their structure-property

relationship. We believe that this finding will open a new avenue in the rational design of MMMs for gas separation.

## MATERIALS AND METHODS

### Chemical and materials

Zirconium(IV) chloride ( $\text{ZrCl}_4$ ; 98%; Alfa Aesar), 2-aminoterephthalic acid ( $\text{NH}_2$ -BDC; 98%; Tokyo Chemical Industry), chromium(III) nitrate nonahydrate [ $\text{Cr}(\text{NO}_3)_3 \cdot 9\text{H}_2\text{O}$ ; 98.5%; SCRC], acetic anhydride ( $\text{Ac}_2\text{O}$ ; 98.5%; SCRC), triethylamine (TEA; 99%; Aladdin), acetic acid glacial (HOAc; 99.5%; Aladdin), DCM (99.5%; Greagent), ethanol (99.7%; Greagent), DMF (99.5%; SCRC), 4,4'-(hexafluoroisopropylidene)diphthalic anhydride (6FDA; 99%; TCI), and 4,4'-oxydiphthalic anhydride (ODPA; 99%; Adamas) were purified by recrystallization in  $\text{Ac}_2\text{O}$  before use. DAM (98%; Adamas) was purified by recrystallization in ethanol. DABA (98%; Adamas) was purified by recrystallization in deionized (DI) water. Matrimid@5218 was purchased from BASF SE. Nitrogen (purity, 99.999%), methane (purity, 99.99%), and carbon dioxide (purity, 99.995%) were purchased from Shanghai Youjiali Liquid Helium Co.

### Synthesis of $\text{UiO-66-NH}_2$ nanoparticles

$\text{UiO-66-NH}_2$  ( $88 \pm 12$  nm) was synthesized according a reported method (42). First, 448 mg of  $\text{ZrCl}_4$  (2.08 mmol) and 376 mg of  $\text{NH}_2$ -BDC (2.08 mmol) were individually dissolved in 60 ml of DMF and then mixed with 7.6 ml of acetic acid (64 equivalent to  $\text{ZrCl}_4$ ). The mixture was heated in an oven at  $120^\circ\text{C}$  for 20 hours. After cooling down to room temperature, the product was collected by centrifugation and washed with fresh DMF and methanol (MeOH) three times, respectively. By increasing the acetic acid to 11.9 and 15.2 ml, the size of the  $\text{UiO-66-NH}_2$  particles can be systematically increase to  $180 \pm 30$  and  $320 \pm 50$  nm, respectively.

### Synthesis of $\text{UiO-66}$ nanoparticles

$\text{ZrCl}_4$  (448 mg and 2.08 mmol) and  $\text{H}_2\text{BDC}$  (345 mg and 2.08 mmol) were dissolved in 85 ml DMF containing 7.6 ml of acetic acid in a glass vial. The vial was capped and placed at  $120^\circ\text{C}$  for 7 hours. The crystals were collected by centrifugation washed with fresh DMF and MeOH three times, respectively.

### Synthesis of MOF-801 nanoparticles

MOF-801 was synthesized by dissolving  $\text{ZrCl}_4$  (699 mg and 3.00 mmol) and fumaric acid (348 mg and 3.00 mmol) in 100 ml of DMF. Then, 6.9 ml of acetic acid and 0.3 ml of triethylamine were added to the solution. The mixture was heated in an oven at  $85^\circ\text{C}$  for 24 hours. After cooling down to room temperature, the product was collected through centrifugation and washed by fresh DMF and MeOH three times, respectively.

### Synthesis of MIL-101(Cr)- $\text{NH}_2$ nanoparticles

$\text{Cr}(\text{NO}_3)_3 \cdot 9\text{H}_2\text{O}$  (600 mg and 1.50 mmol) and  $\text{NH}_2$ -BDC (271 mg and 1.50 mmol) were dispersed in 30.0 ml of DI water and then mixed with 62.5  $\mu\text{l}$  of hydrochloric acid [0.5 equivalent to  $\text{Cr}(\text{NO}_3)_3 \cdot 9\text{H}_2\text{O}$ ]. The mixture was then transferred to a 50.0-ml Teflon-lined autoclave and heated in a  $120^\circ\text{C}$  oven for 24 hours. After cooling down to room temperature, the product was collected by centrifugation, washed with 20 ml of DI water two times, and soaked in DMF overnight at  $80^\circ\text{C}$  to remove the excess  $\text{NH}_2$ -BDC.

### Synthesis of ODPA-DAM and 6FDA-DAM

ODPA-DAM and 6FDA-DAM polymer were synthesized through the condensation reaction between dianhydrides and diamines, followed by a chemical imidization step (39). A total of 2.40 g (16.00 mmol) DAM and anhydrous DMF (15 ml) were added into a 100-ml flask equipped with a nitrogen inlet. The mixture was cooled to  $0^\circ\text{C}$  and then 4.96/7.11 g (16.00 mmol) ODPA/6FDA and anhydrous DMF (15 ml) were added. The solution was stirred for 24 hours to form a polyamide acid. For imidization, a solution of 2.2 ml of TEA and 5.4 ml of  $\text{Ac}_2\text{O}$  mixed in 5.0 ml of anhydrous DMF was added. The mixture was vigorously stirred for 24 hours to obtain a fully cyclized polyimide. White polyimide beads were isolated by dropwise addition of the viscous polymer solution into stirring MeOH. The polyimide was washed with MeOH several times, soaked in fresh MeOH overnight, and dried in a vacuum oven at  $150^\circ\text{C}$  for 24 hours.

### Synthesis of RCP

Synthesis of the copolymers was performed similarly to that of the pure polyimide, ODPA-DAM. However, instead of adding equimolar amounts of ODPA and DAM to the reaction vessel, a mixture of ODPA and 6FDA was used for polymerization. The molar ratio between the total dianhydride and diamine was kept at 1:1.

The syntheses of RCPs were as follows: For ( $\text{ODPA}_{0.67}/6\text{FDA}_{0.33}$ )-DAM (P1), 2.40 g (16.00 mmol) of DAM, 3.31 g (10.67 mmol) of ODPA, and 2.37 g (5.33 mmol) of 6FDA were used for polymerization. For ( $\text{ODPA}_{0.50}/6\text{FDA}_{0.50}$ )-DAM (P2), 2.40 g (16.00 mmol) of DAM, 2.48 g (8.00 mmol) of ODPA, and 3.56 g (8.00 mmol) of 6FDA were used for polymerization. For ( $\text{ODPA}_{0.33}/6\text{FDA}_{0.67}$ )-DAM (P3), 2.40 g (16.00 mmol) of DAM, 1.65 g (5.33 mmol) of ODPA, and 4.74 g (10.67 mmol) of 6FDA were used for polymerization. For ( $\text{ODPA}_{0.25}/6\text{FDA}_{0.75}$ )-DAM (P4), 2.40 g (16.00 mmol) of DAM, 1.24 g (4.00 mmol) of ODPA, and 5.34 g (12.00 mmol) of 6FDA were used for polymerization. For 6FDA-(DAM<sub>0.85</sub>/DABA<sub>0.15</sub>), 2.04 g (13.60 mmol) of DAM, 0.365 g (2.40 mmol) of DABA, and 7.11 g (16.00 mmol) of 6FDA were used for polymerization. For all reactions, a solution of 16.00 mmol of TEA and 80.00 mmol of  $\text{Ac}_2\text{O}$  dissolved in 5 ml of DMF was added for imidization.

### Preparation of pure polyimide membranes

To prepare neat ODPA-DAM, 6FDA-DAM, P1, and P4 membranes, a 5 wt% polyimide (ODPA-DAM, 6FDA-DAM, P1, or P4) solution in DCM was prepared and filtered through a 0.45- $\mu\text{m}$  polytetrafluoroethylene (PTFE) filter onto a casting tray. The tray consists of a glass ring attached to a leveled quartz plate by epoxy sealant. After slow evaporation of the solvent, the membrane was peeled off from the quartz plate and dried overnight in a vacuum oven to remove residual solvent.

### Preparation of polymer blend membranes

A polymer solution was prepared by dissolving 200 mg of dry polyimide (ODPA-DAM, 6FDA-DAM, P1, P2, or P3) in 4 ml of DCM. Then, two polymer solutions were mixed at 1:1 volumetric ratio and stirring for 30 min. The solution was casted on a flat quartz plate. After evaporation of solvent, the membrane was peeled off from the glass plate and dried overnight to remove residual solvent.

### Preparation of mixed-matrix membranes

To fabricate MMMs, UiO-66-NH<sub>2</sub> particles were centrifuged from DCM and then mixed with a 5 wt% polymer or polymer blend solution in DCM. The solutions were sonicated by a probe sonicator for 1 min before casting on a flat quartz plate. After evaporation of the solvent, the membrane was peeled off from the glass plate and dried overnight in a vacuum oven to remove residual solvent. Before gas permeation measurement, membranes were thermally treated at 150°C for 20 hours under dynamic vacuum to remove any residual solvent.

### Preparation of TFC membrane

To fabricate TFC membrane, UiO-66-NH<sub>2</sub> particles were centrifuged from DCM and then mixed with a 2 wt% polymer blend solution (ODPA-DAM/6FDA-DAM) in DMF/DCM (20/80 by volume). This mixture was stirred for 30 min in an oil bath at 40°C. Then, a silicon wafer was dipped into this mixture for 10 s and withdrawn with 1 mm/s. The membrane was kept at room temperature for 1 day for complete solvent evaporation.

### Material characterization

TEM images were acquired on a JEM 1400 field-emission TEM with voltage set at 120 kV. EDS elemental mapping images were collected on a JEM F200 plus (200 kV). SEM images were acquired on a JEOL JSM 7800F Prime SEM. PXRD was acquired on a Bruker D8 Advance diffractometer with Cu K $\alpha$  radiation. TGA experiments were performed on a PerkinElmer TGA 8000. Samples were first heated to 150°C and kept at that temperature for 30 min under N<sub>2</sub> atmosphere to remove residual solvent. Then, the temperature was increased to 700°C at a rate of 20°C/min under O<sub>2</sub> atmosphere and kept at 700°C for 10 min. The temperature was then raised to 750°C at a rate of 20°C/min before termination of the program. For ultramicrotomy, samples were first embedded into epoxy resin (EPON 812; Sigma-Aldrich) and cured at 60°C for 24 hours. Ultrathin slices with thickness of 100 nm were obtained on a Leica EM UC7 ultramicrotome. High-pressure CO<sub>2</sub>/CH<sub>4</sub> adsorption isotherms were measured on an iSorBHP1 instruments from Quantachrome. <sup>1</sup>H NMR (nuclear magnetic resonance) spectra were collected on a Bruker AVANCE III HD 400-MHz spectrometer. Gel permeation chromatography (GPC) experiments were carried out on a Malvern TDA305 Multiple Detector (light scattering, refractive index, and ultraviolet) and calibrated using polymethyl methacrylate (PMMA) standards. Tensile testing was performed on an Instron 5960 at a pulling rate of 1 mm/min; three samples were tested for each experiment, and the samples were cut into rectangle shape that were 6 mm wide and approximately 25 mm long.

### NMR characterization of synthesized polymers

Copolymer compositions were confirmed by <sup>1</sup>H NMR. Peaks at 1.98 and 2.21 parts per million (ppm; nine methyl protons from DAM), 7.51 and 7.55 ppm (four aromatic protons from ODPA), and 7.94 ppm (four aromatic protons from 6FDA) were integrated and used to calculate monomer ratios. Table S4 shows good agreement between the targeted ratios, and the ratios were calculated from NMR data. Therefore, targeted ratios were used in the manuscript.

### Gas permeability measurements

The single gas permeation was performed at 35°C and 3 bar with a home-built variable-pressure constant-volume setup. Membranes

were activated by heating at 100°C under high vacuum overnight before testing. Then, the preactivated membrane was placed on the central hole of a custom-made brass disk sealed by heat-resistant epoxy resin and then housed in a membrane cell. The upstream pressure was monitored by a high-accuracy gauge. Downstream was kept under vacuum until measurement. In a typical permeation measurement experiment, the entire permeation system was degassed under high vacuum for at least 3 hours. Then, the leak rate of downstream was determined by measuring the pressure increment within 10 min with the vacuum valve closed. The leak test was performed for at least two times. Permeation was measured for 3 min at each pressure point. The permeability value was obtained by averaging the measurement from three membrane samples at the same pressure point. The permeability can be calculated by Eq. 1

$$P = \frac{IV_{\text{cell}}}{A\Delta p RT} \left[ \left( \frac{dp}{dt} \right)_{\text{SS}} - \left( \frac{dp}{dt} \right)_{\text{leak}} \right] \quad (1)$$

where  $P$  is the permeability [1 Barrer = 10<sup>-10</sup> cm<sup>3</sup> (STP) cm cm<sup>-2</sup> s<sup>-1</sup> cmHg<sup>-1</sup>],  $l$  is the thickness of the film,  $A$  is the effective area of the membrane,  $V_{\text{cell}}$  is the downstream volume,  $T$  is the operating temperature in kelvin,  $(dp/dt)_{\text{SS}}$  is the steady-state permeation rate, and  $(dp/dt)_{\text{leak}}$  is the leak rate.  $\Delta p$  is the pressure difference between upstream and downstream.  $R$  is the ideal gas constant.

The ideal selectivity of pure gas A and B can be calculated by using Eq. 2

$$\alpha = \frac{P_A}{P_B} \quad (2)$$

where  $P_A$  and  $P_B$  are the permeability of pure gas A and B, respectively.

### Permeability, solubility, and diffusivity (47)

To further elucidate the mechanism of increased selectivity and permeability, permeability is expressed as the product of the average effective diffusivity ( $D$ ) and solubility ( $S$ ) of the gas within the membrane

$$P = D \cdot S \quad (3)$$

The solubility represents the thermodynamic contribution to transport, and it also related to the equilibrium adsorption isotherm (Eq. 4)

$$S = \frac{\rho n_o}{p_o} \quad (4)$$

where  $\rho$  is the density of the membrane in g cm<sup>-3</sup>,  $n_o$  is the amount adsorbed in equilibrium with the feed pressure in cm<sup>3</sup>(STP) g<sup>-1</sup> and measured from the adsorption isotherm, and  $p_o$  is the feed pressure in mbar. The density of the membrane was calculated using the crystallographic density of the framework (48), the density of the polymer, and the mass loading of MOF in the polymer as measured by TGA. The diffusivity can then be calculated using  $D=P/S$ .

### Calculation details

#### Quantifying the MOF particles dispersibility in polymer matrix (43, 45)

The quality of the MOF dispersion in polymer matrixes can be evaluated by the DFPS between MOF particles. The more uniform the

spacing between MOF particles (surface-to-surface distance), the closer the spacing distribution frequency is to the normal distribution. In contrast, the more MOF particles aggregate, the smaller the spacing between MOF particles, and the maxima of DFPS will appear close to zero. The dispersion of MOF particles in polymer matrix was analyzed quantitatively on the basis of TEM images. First, 30 equal distance horizontal or vertical grid lines were overlaid onto the TEM images. Then, the free path spacing between adjacent MOF particles were accurately measured (fig. S20). The number of measurements  $N$  was about 250 for each sample. Next, these values were plotted into a histogram.

The frequency density  $f$  of each scenario is thus

$$f = \frac{n_i}{N\Delta x} \quad (5)$$

where  $n_i$  is the number of data falling into this group,  $N$  is the total number of the measurements, and  $\Delta x$  is the spacing interval.

### Quantifying the local packing density of MOF particles in MMMs

The packing density of MOFs in MMM was quantitatively analyzed and calculated using ImageJ software (49). In the ImageJ window of MMM image, a boundary of a MOF domain and the domain area were manually defined and calculated using the lasso tool. A threshold range is set to distinguish the MOF particles from the polymer matrix. All pixels in the image with values below the threshold are converted to red (fig. S15). The packing density of MOF particles can be calculated by measuring their area fraction within polymer domains or MOF domains.

## Supplementary Materials

This PDF file includes:

Figs. S1 to S23  
Tables S1 to S5

## REFERENCES AND NOTES

- D. S. Sholl, R. P. Lively, Seven chemical separations to change the world. *Nature* **532**, 435–437 (2016).
- P. Angelini, T. Armstrong, R. Counce, W. Griffith, T. LKlasson, G. Muralidharan, C. Narula, V. Sikka, G. Closset, G. Keller, *Materials for separation technologies: Energy and emission reduction opportunities* (DOE, 2005), p. 103.
- K. Sorschak, XEBEC Investor Presentation First Quarter 2017; www.paulbenwell.com/wp-content/uploads/2017/06/IR-Presentation-June-16-2017.pdf.
- R. W. Baker, *Membrane Technology and Applications* (John Wiley & Sons, 2012).
- H. B. Park, J. Kamcev, L. M. Robeson, M. Elimelech, B. D. Freeman, Maximizing the right stuff: The trade-off between membrane permeability and selectivity. *Science* **356**, eaab0530 (2017).
- L. M. Robeson, Correlation of separation factor versus permeability for polymeric membranes. *J. Membr. Sci.* **62**, 165–185 (1991).
- L. M. Robeson, The upper bound revisited. *J. Membr. Sci.* **320**, 390–400 (2008).
- R. D. Noble, Perspectives on mixed matrix membranes. *J. Membr. Sci.* **378**, 393–397 (2011).
- G. Dong, H. Li, V. Chen, Challenges and opportunities for mixed-matrix membranes for gas separation. *J. Mater. Chem. A* **1**, 4610 (2013).
- M. Galizia, W. S. Chi, Z. P. Smith, T. C. Merkel, R. W. Baker, B. D. Freeman, *50th Anniversary Perspective: Polymers and mixed matrix membranes for gas and vapor separation: A review and prospective opportunities*. *Macromolecules* **50**, 7809–7843 (2017).
- J. Dechnik, J. Gascon, C. J. Doonan, C. Janiak, C. J. Sumby, Mixed-matrix membranes. *Angew. Chem. Int. Ed.* **56**, 9292–9310 (2017).
- S. Wang, X. Li, H. Wu, Z. Tian, Q. Xin, G. He, D. Peng, S. Chen, Y. Yin, Z. Jiang, M. D. Guiver, Advances in high permeability polymer-based membrane materials for CO<sub>2</sub> separations. *Energ. Environ. Sci.* **9**, 1863–1890 (2016).
- W. Xu, B. Tu, Q. Liu, Y. Shu, C.-C. Liang, C. S. Diercks, O. M. Yaghi, Y.-B. Zhang, H. Deng, Q. Li, Anisotropic reticular chemistry. *Nat. Rev. Mater.* **5**, 764–779 (2020).
- Z. Ji, H. Wang, S. Canossa, S. Wuttke, O. M. Yaghi, Pore chemistry of metal-organic frameworks. *Adv. Funct. Mater.* **30**, 2000238 (2020).
- H.-C. J. Zhou, S. Kitagawa, Metal-organic frameworks (MOFs). *Chem. Soc. Rev.* **43**, 5415–5418 (2014).
- S. Yuan, L. Feng, K. Wang, J. Pang, M. Bosch, C. Lollar, Y. Sun, J. Qin, X. Yang, P. Zhang, Q. Wang, L. Zou, Y. Zhang, L. Zhang, Y. Fang, J. Li, H. Zhou, Stable metal-organic frameworks: Design, synthesis, and applications. *Adv. Mater.* **30**, 1704303 (2018).
- L. J. Murray, M. Dincă, J. R. Long, Hydrogen storage in metal-organic frameworks. *Chem. Soc. Rev.* **38**, 1294 (2009).
- R.-B. Lin, S. Xiang, B. Li, Y. Cui, G. Qian, W. Zhou, B. Chen, Our journey of developing multifunctional metal-organic frameworks. *Coord. Chem. Rev.* **384**, 21–36 (2019).
- H. B. Tanh Jeazet, C. Staudt, C. Janiak, Metal-organic frameworks in mixed-matrix membranes for gas separation. *Dalton Trans.* **41**, 14003 (2012).
- G. Liu, V. Chernikova, Y. Liu, K. Zhang, Y. Belmabkhout, O. Shekhat, C. Zhang, S. Yi, M. Eddaoudi, W. J. Koros, Mixed matrix formulations with MOF molecular sieving for key energy-intensive separations. *Nat. Mater.* **17**, 283–289 (2018).
- M. Kalaj, K. C. Bentz, S. Ayala Jr., J. M. Palomba, K. S. Barcus, Y. Katayama, S. M. Cohen, MOF-polymer hybrid materials: From simple composites to tailored architectures. *Chem. Rev.* **120**, 8267–8302 (2020).
- S. J. Datta, A. Mayoral, N. Murthy Srivatsa Bettahalli, P. M. Bhatt, M. Karunakaran, I. D. Carja, D. Fan, P. G. M. Mileo, R. Semino, G. Maurin, O. Terasaki, M. Eddaoudi, Rational design of mixed-matrix metal-organic framework membranes for molecular separations. *Science* **376**, 1080–1087 (2022).
- Q. Qian, P. A. Asinger, M. J. Lee, G. Han, K. Mizrahi Rodriguez, S. Lin, F. M. Benedetti, A. X. Wu, W. S. Chi, Z. P. Smith, MOF-based membranes for gas separations. *Chem. Rev.* **120**, 8161–8266 (2020).
- H. Wang, S. He, X. Qin, C. Li, T. Li, Interfacial engineering in metal-organic framework-based mixed matrix membranes using covalently grafted polyimide brushes. *J. Am. Chem. Soc.* **140**, 17203–17210 (2018).
- C. Wu, K. Zhang, H. Wang, Y. Fan, S. Zhang, S. He, F. Wang, Y. Tao, X. Zhao, Y.-B. Zhang, Y. Ma, Y. Lee, T. Li, Enhancing the gas separation selectivity of mixed-matrix membranes using a dual-interfacial engineering approach. *J. Am. Chem. Soc.* **142**, 18503–18512 (2020).
- C. M. Zimmerman, A. Singh, W. J. Koros, Tailoring mixed matrix composite membranes for gas separations. *J. Membr. Sci.* **137**, 145–154 (1997).
- I. Kiesow, D. Marczewski, L. Reinhardt, M. Mühlmann, M. Possiwan, W. A. Goedel, Bicontinuous zeolite polymer composite membranes prepared via float casting. *J. Am. Chem. Soc.* **135**, 4380–4388 (2013).
- X. Ma, X. Wu, J. Caro, A. Huang, Polymer composite membrane with penetrating ZIF-7 sheets displays high hydrogen permselectivity. *Angew. Chem. Int. Ed.* **131**, 16302–16306 (2019).
- N. C. Su, D. T. Sun, C. M. Beavers, D. K. Britt, W. L. Queen, J. J. Urban, Enhanced permeation arising from dual transport pathways in hybrid polymer-MOF membranes. *Energ. Environ. Sci.* **9**, 922–931 (2016).
- W. S. Chi, B. J. Sundell, K. Zhang, D. J. Harrigan, S. C. Hayden, Z. P. Smith, Mixed-matrix membranes formed from multi-dimensional metal-organic frameworks for enhanced gas transport and plasticization resistance. *ChemSusChem* **12**, 2355–2360 (2019).
- J. H. Jo, C. O. Lee, G. Y. Ryu, H. Jae, D. Roh, W. S. Chi, Hierarchical amine-functionalized ZIF-8 mixed-matrix membranes with an engineered interface and transport pathway for efficient gas separation. *ACS Appl. Polym. Mater.* **4**, 6426–6439 (2022).
- M. J. C. Ordoñez, K. J. Balkus, J. P. Ferraris, I. H. Musselman, Molecular sieving realized with ZIF-8/Matrimid mixed-matrix membranes. *J. Membr. Sci.* **361**, 28–37 (2010).
- E. M. Mahdi, J.-C. Tan, Mixed-matrix membranes of zeolitic imidazolate framework (ZIF-8)/Matrimid nanocomposite: Thermo-mechanical stability and viscoelasticity underpinning membrane separation performance. *J. Membr. Sci.* **498**, 276–290 (2016).
- Z. P. Smith, J. E. Bachman, T. Li, B. Gludovatz, V. A. Kusuma, T. Xu, D. P. Hopkinson, R. O. Ritchie, J. R. Long, Increasing M<sub>2</sub>(dobdc) loading in selective mixed-matrix membranes: A rubber toughening approach. *Chem. Mater.* **30**, 1484–1495 (2018).
- D. Dai, H. Wang, C. Li, X. Qin, T. Li, A Physical entangling strategy for simultaneous interior and exterior modification of metal-organic framework with polymers. *Angew. Chem. Int. Ed.* **133**, 7465–7472 (2021).
- B. Seoane, J. Coronas, I. Gascon, M. E. Benavides, O. Karvan, J. Caro, F. Kapteijn, J. Gascon, Metal-organic framework based mixed matrix membranes: A solution for highly efficient CO<sub>2</sub> capture? *Chem. Soc. Rev.* **44**, 2421–2454 (2015).
- R. Lin, B. Villacorta Hernandez, L. Ge, Z. Zhu, Metal organic framework based mixed matrix membranes: An overview on filler/polymer interfaces. *J. Mater. Chem. A* **6**, 293–312 (2018).
- Z. Wang, D. Wang, S. Zhang, L. Hu, J. Jin, Interfacial design of mixed matrix membranes for improved gas separation performance. *Adv. Mater.* **28**, 3399–3405 (2016).

39. W. Qiu, L. Xu, C.-C. Chen, D. R. Paul, W. J. Koros, Gas separation performance of 6FDA-based polyimides with different chemical structures. *Polymer* **54**, 6226–6235 (2013).
40. J. H. Cavka, S. Jakobsen, U. Olsbye, N. Guillou, C. Lamberti, S. Bordiga, K. P. Lillerud, A new zirconium inorganic building brick forming metal organic frameworks with exceptional stability. *J. Am. Chem. Soc.* **130**, 13850–13851 (2008).
41. B. Ghalei, K. Sakurai, Y. Kinoshita, K. Wakimoto, A. P. Isfahani, Q. Song, K. Doitomi, S. Furukawa, H. Hirao, H. Kusuda, S. Kitagawa, E. Sivaniah, Enhanced selectivity in mixed matrix membranes for CO<sub>2</sub> capture through efficient dispersion of amine-functionalized MOF nanoparticles. *Nat. Energy* **2**, 17086 (2017).
42. A. Schaate, P. Roy, A. Godt, J. Lippke, F. Waltz, M. Wiebcke, P. Behrens, Modulated synthesis of Zr-based metal–organic frameworks: From nano to single crystals. *Chem. A Eur. J.* **17**, 6643–6651 (2011).
43. Z. P. Luo, J. H. Koo, Quantifying the dispersion of mixture microstructures. *J. Microsc.* **225**, 118–125 (2007).
44. B. M. Tyson, R. K. Abu Al-Rub, A. Yazdanbakhsh, Z. Grasley, A quantitative method for analyzing the dispersion and agglomeration of nano-particles in composite materials. *Compos. B. Eng.* **42**, 1395–1403 (2011).
45. C. Li, J. Liu, K. Zhang, S. Zhang, Y. Lee, T. Li, Coating the right polymer: Achieving ideal metal–organic framework particle dispersibility in polymer matrixes using a coordinative crosslinking surface modification method. *Angew. Chem. Int. Ed.* **133**, 14257–14264 (2021).
46. J. G. Wijmans, R. W. Baker, The solution-diffusion model: A review. *J. Membr. Sci.* **107**, 1–21 (1995).
47. J. E. Bachman, Z. P. Smith, T. Li, T. Xu, J. R. Long, Enhanced ethylene separation and plasticization resistance in polymer membranes incorporating metal–organic framework nanocrystals. *Nat. Mater.* **15**, 845–849 (2016).
48. B. M. Connolly, M. Aragoes-Anglada, J. Gandara-Loe, N. A. Danaf, D. C. Lamb, J. P. Mehta, D. Vulpe, S. Wuttke, J. Silvestre-Albero, P. Z. Moghadam, A. E. H. Wheatley, D. Fairen-Jimenez, Tuning porosity in macroscopic monolithic metal-organic frameworks for exceptional natural gas storage. *Nat. Commun.* **10**, 2345 (2019).
49. T. Ferreira, W. Rasband, ImageJ user guide. *ImageJ/Fiji* **1**, 155–161 (2012).

#### Acknowledgments

**Funding:** This work was supported by the National Natural Science Foundation of China (grant no. 22075181) and the start-up funding from ShanghaiTech University. We thank the support from Analytical Instrumentation Center (grant no. SPST-AIC10112914), SPST, ShanghaiTech University, and the Center for High-resolution Electron Microscopy (ChEM) of SPST at ShanghaiTech University under grant no. EM02161943. Y.T. and Y.-B.Z. thanks the support of the Science and Technology Commission of Shanghai Municipality (nos. 21XD1402300, 21JC1401700, and 21DZ2260400) and the Double First-Class Initiative Fund of ShanghaiTech University (SYLDX0052022). **Author contributions:** Methodology: C.L. and A.Q. Investigation: C.L., A.Q., Y.L., Y.T., and Y.-B.Z. Supervision: T.L. Writing (original draft): C.L. Writing (review and editing): C.L. and T.L. **Competing interests:** The authors declare that they have no competing interests. **Data and materials availability:** All data needed to evaluate the conclusions in the paper are present in the paper and/or the Supplementary Materials.

Submitted 28 October 2022

Accepted 27 February 2023

Published 31 March 2023

10.1126/sciadv.adf5087